Applied Catalysis B: Environmental 240 (2019) 225–233

Contents lists available at ScienceDirect

Applied Catalysis B: Environmental

journal homepage: www.elsevier.com/locate/apcatb

π–π Interaction between self-assembled perylene diimide and 3D graphene for excellent visible-light photocatalytic activity

Jun Yang[a], Hong Miao[a], Yunxia Wei[b], Wenlu Li[a], Yongfa Zhu[a,*]

[a] Department of Chemistry, Tsinghua University, Beijing, 100084, PR China
[b] College of Chemistry and Chemical Engineering, Lanzhou City University, Lanzhou, 730070, PR China

ARTICLE INFO

Keywords:
Photocatalyst
π–π interaction
Three-dimensional structure
Electron transfer

ABSTRACT

A three-dimensional (3D) graphene/self-assembled perylene imide (rGO/PDI) aerogel composite has been successfully constructed via a simple low-temperature hydrothermal method in this work. The 3D rGO/PDI composite exhibited superior visible-light photocatalytic performance. The removal rate was respectively 2.46 times and 3.33 times higher than that of PDI in static and dynamic catalytic systems. The satisfactory activity is mainly attributed to the more effective separation of electron–hole pairs. To be specific, the self-assembled PDI nanofibers and graphene are effectively combined via non-covalent π-π interaction. The π-π interaction enhances the long-range π-electrons delocalization and electron coupling effects, which is beneficial for the carrier mobility and the separation of electron–hole pairs. Meanwhile, the three-dimensional structure of graphene provides a fast multidimensional channel for electron transfer and effectively improves the adsorption capacity of PDI due to the large specific surface area. What's more, the rGO/PDI composite exhibits great stability than the pure PDI. Overall, this work provides a new insight into improving the photocatalytic activity of self-assembled organic materials.

1. Introduction

In recent years, the problem of water contamination is becoming an overwhelming problem all over the world. Photocatalytic oxidation technology has shown tremendous potential as a promising avenue in water treatment because of its environmental friendliness, good cost-eff ;ectiveness and high efficiency [1–5]. Among various photocatalysts, organic photocatalytic materials have received widespread attention for their flexible designs, various chemical structures, low costs and rich origin of elements [6,7]. At present, the research for organic photocatalyst is mainly focused on organometallic complexes [8–10] and covalent organic polymers [11–14]. But their widespread applications in the field of photocatalysis are largely limited because of the potential toxicity, complicated synthetic process and high cost. Based on this, it is the key to find ecofriendly organic photocatalyst materials with high photocatalytic activity.

Recently, self-assembled supramolecular organic materials have shown great potential in the field of photocatalysis, such as diketopyrrolopyrrole (DPP) [15,16], porphyrin (TPP) [17–19], perylene monoimide (PMI) [20,21] and perylene imide (PDI) [22]. They have been applied in light-driven water splitting, photocatalytic degradation and organic photosynthesis. In particular, perylene imide and its derivatives, as a typical n-type organic semiconductor, have been applied in photocatalysis because of their high photo-thermal stability, excellent charge mobility and electron affinity [23–28]. However, it suffers from the problems of easy recombination of photo-generated carriers, low adsorption capacity and low recycling rate for their poor stability in the photocatalytic process. These defects greatly limit their photocatalytic applications. Currently, the modification research of self-assembled PDI is mainly focused on introducing functional groups [24], forming short-range π-π stacking structure [22], and adjusting electron acceptor and donor units [26]. These methods are intended to improve the electron transfer rate via increasing the built-in electric field of self-assembled PDI. However, the preparation process of these methods are complicated and it is negligible for the improvement of its stability and adsorption capacity. Therefore, it is very important to seek an efficient modification method for organic supramolecular self-assembled photocatalysts.

Currently, the three-dimensional (3D) structure carbon materials exhibit many advantages over their one-dimensional and two-dimensional structures because of the larger specific surface area, lower sheet agglomeration and higher thermal/electrical stability [29]. The three-dimensional structure materials have been applied in many fields, such as battery materials [30], biosensors [31] and photocatalysis [32–34].

* Corresponding author.
E-mail address: zhuyf@mail.tsinghua.edu.cn (Y. Zhu).

https://doi.org/10.1016/j.apcatb.2018.09.003
Received 2 July 2018; Received in revised form 28 August 2018; Accepted 2 September 2018
Available online 05 September 2018

In the last few years, a variety of three-dimensional structure photocatalysts have been successfully synthesized, such as PANI/g-C_3N_4 [35], g-C_3N_4/Agar [36], g-C_3N_4 /SiO_2 [37], PANI/TiO_2 [38] and TiO_2-graphene [39]. Among numerous three-dimensional network structure materials, graphene-based composite photocatalysts have received extensive attention for their high adsorption ability and easy circulation. Importantly, the excellent conductivity of graphene can effectively promote the electron transfer and its three-dimensional mesoporous structure provides a multidimensional channel for mass transfer and electron transport in catalytic reactions [40,41]. The advantages are very favorable for photocatalytic reactions. At present, the research on 3D graphene-based composites mainly focuses on graphene/inorganic semiconductors [42,43], but such materials have the disadvantages of high cost, poor interface contact effect, and complicated preparation process. Fortunately, constructing the graphene-supramolecular self-assembled organic photocatalysts may be able to overcome these disadvantages. In addition, considering the deficiencies of PDI as stated above, it may be a good choice to construct a graphene-supported three-dimensional structure to improve the photocatalytic performance of PDI.

Based on the above analysis, a three-dimensional graphene/self-assembled perylene imide (rGO/PDI) aerogel composite was successfully constructed via a simple low-temperature hydrothermal method (Scheme 1). The 3D rGO/PDI composite exhibited a satisfactory photocatalytic activity under visible light irradiation. The excellent activity is mainly attributed to the close π-π interaction between PDI and graphene, which greatly facilitated the separation of electron–hole pairs. In addition, the three-dimensional structure effectively improves the adsorption capacity of PDI. In a word, our work provides a new idea for the modification of self-assembled supramolecular organic photocatalysts.

2. Experimental section

2.1. The synthesis of rGO/ PDI aerogel composite

The self-assembled perylene diimide (PDI) was synthesized by the previous work and was described in detail in the supporting file [24,25]. GO was prepared from graphite powder according to Hummer's method [44]. Firstly, a stock solution of 200.0 mL of N, *N*-di (propanoic acid)-perylene-3,4,9,10-tetracarboxylic diimide (5.0 mM) was prepared with addition of 834 μL of triethylamine solution under vigorous stirring. Subsequently, the solution of 4.0 M HCl (5.62 ml) was added into the red stock solution (37.45 ml, containing PDI 100 mg) and then stirred for three hours. A certain volume of GO stock solution (1 mg/ml) was added under stirring and then ultrasound for 2 h. Then, a given mass of ascorbic acid was added under stirring followed ultrasound for another 2 h. The resulting mixture further heated for 4 h at 95 °C in a water bath. The as-prepared hydrogels were washed with distilled water until the pH of filtrate became neutral and then freeze-dried to obtain aerogels, which were denoted as rGO/PDI-X. (rGO/PDI-X, X represented the mass fraction of PDI in the composite system. X = 40%,50%, 55%, 57%, 60%, 63%, 65%, 67%, 70%, 80%, 90%)

2.2. Characterization of materials

The X-ray powder diffraction (XRD) data were recorded at room temperature by a Bruker D8 Advance X-ray diffractometer at 40 kV and 40 mA for monochromatized Cu Kα (λ = 1.5406 Å) radiation. The morphologies of the samples were determined with the scanning electron microsopy (FE-SEM, Hitachi SU-8010), the transmission electron microscope (TEM, Hitachi HT 7700) and the atomic force microscopy (AFM, SPM-9700). The optical diffuse reflectance spectra were measured by Hitachi U-3010 spectrophotometer and $BaSO_4$ was used as the reference. Fourier transfer infrared (FT-IR) spectra were carried out using the Bruker V70 spectrometer. Raman spectra were measured on the microscopic confocal Raman spectrometer (HORIBA HR800) with an excitation of 514 nm laser light. The photoluminescence (PL) spectra were performed by using an Edinburgh FS5 spectrophotometer with an excitation wavelength of 612 nm. X-ray photoelectron spectroscopy (XPS) was performed on the ULVAC-PHI-Quantera spectrometer. A Micromeritics ASAP2020 Surface Area and Porosity Analyzer were used to measure the surface areas of the samples at liquid nitrogen temperature (77 K). The photocurrent experiments were performed by using the electrochemical workstation (CHI-660E, China). The detection of the active species was performed on the JES-FA200 EPR Spectrometer paramagnetic resonance spectrometer.

2.3. Photocatalytic activity test

The photocatalytic performances in static system were evaluated by degrading phenol (5 ppm) in a multi-tube agitated reactor under visible light irradiation (λ > 420 nm). The visible light source was used with a 500 W xenon lamp (filter, λ = 420 nm) with an average light intensity of 27 mW/cm^2. In detail, 25 mg of photocatalyst was dispersed in a quartz tube containing 50 ml phenol aqueous solution (5 ppm) and the suspension was kept stirring in the dark for 1 h to reach the adsorption-desorption equilibrium on the catalyst surface. Then the suspension was irradiated by the 500 W xenon lamp (λ > 420 nm). After that, 2 mL of the suspension was extracted at given intervals. The concentration of phenol was detected by a high performance liquid chromatography (HPLC) system and the detection wavelength of phenol was 270 nm. In

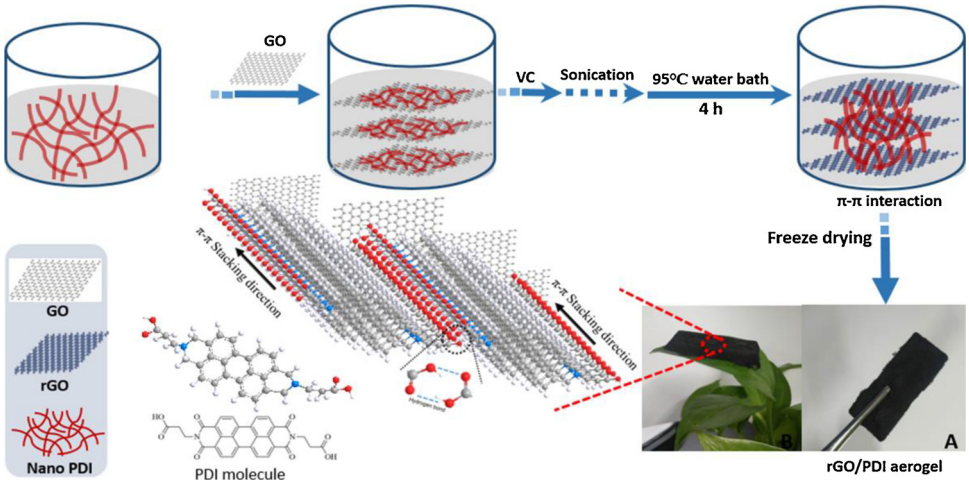

Scheme 1. Schematic illustration of the synthesis of 3D rGO/PDI composite aerogel.

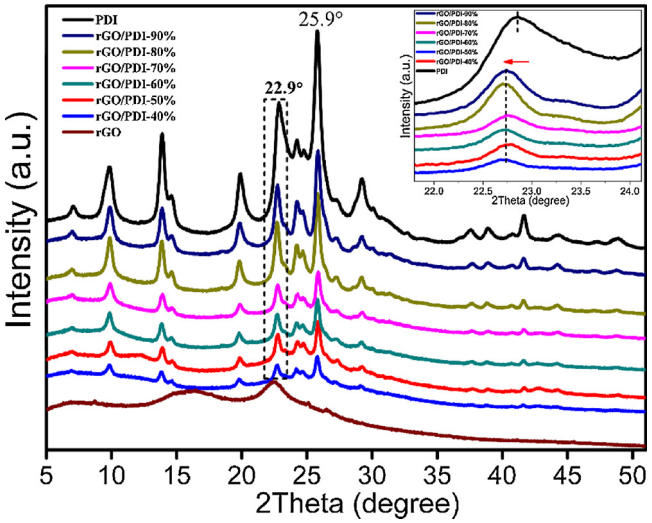

Fig. 1. XRD patterns of rGO, PDI and rGO/PDI-X (rGO/PDI-X, X represents the mass fraction of PDI in the composite system).

addition, the photocatalytic experiments in dynamic system was described in detail in the supporting file.

3. Results and discussion

3.1. The π−π interaction between rGO and PDI

The preparation process of the 3D rGO/PDI aerogel composite was illustrated in Scheme 1. Before the hydrothermal reaction, nano PDI and graphene oxide (GO) aqueous solution were mixed sufficiently, which enabled the PDI to be adsorbed eff ;ectively on the surface of GO due to the π-π interactions between them [45–47]. Subsequently, the most of hydrophilic oxygen-containing functional groups of GO were removed via the hydrothermal reaction to form reduced GO (rGO), which could recover the π-π conjugation between layers [48]. Meanwhile the residual hydrophilic groups could absorb water via hydrogen bonding, which can prevent parallel stacking of rGO sheets, helping to form the 3D structure [49].

Fig. 1 shows the XRD patterns of the as-prepared samples. It can be seen that rGO shows a broad peak of (002) at 2θ = 22.4°, which corresponds to a layer-to-layer spacing of 3.5 Å. The diffraction peaks of rGO are wide and weak, which indicates that interlayer peeling occurs with the reduction of graphene oxide and it may form a thin layer or even a single layer. As for the self-assembled PDI, it has a clear π-π stacking peak at 2θ = 25.9°, corresponding to its lattice spacing of 3.4 Å [50]. It is interesting that the typical d-spacing of π-π stacking of PDI is similar to the layer-to-layer spacing of graphene, which provides a useful condition for the generation of π-π interactions between them. The enlargement of electron delocalization effect is beneficial to facilitate charge transfer. For all the composites, the intensities of the diffraction peaks of PDI increase with its increasing mass fraction. In addition, it can be seen that the diffraction peaks of the composites shifted toward low angles compared to the self-assembled PDI, which indicates the existence of π-π interactions between them.

To further illustrate the π-π interaction between rGO and PDI, Raman and infrared measurements were performed. As shown in the Fig. 2(A), it can be seen that there are two main peaks of graphene, namely the disordered peak (marked as D peak, 1350 cm^{-1}) and the graphite peak (marked as G peak, 1586 cm^{-1}). It is obvious that the I_D/I_G value of rGO (1.25) is higher than that of GO (0.94), indicating that the oxygen-containing groups are largely reduced [51,52]. As for PDI, the peak of 1582 cm^{-1} is attribute to the stretching vibration of C=C/C−C, which is sensitive to the π-π stacking interactions. However, the 1296 cm^{-1} peak is insensitive to the π-π stacking effect corresponding to the CH in plane bending. Therefore, the intensity ratio of 1582 cm^{-1}/1296 cm^{-1} can be used to evaluate the degree of π–π stacking [52]. It turns out that the intensity ratio of rGO/PDI is 0.86, which is even higher than that of PDI (0.69). This indicates that the addition of graphene does not affect the π-π stacking of PDI and the similar stack spacing even promotes the degree of ordered π-π stacking. The coplanar π-π stacking along the long axis of the PDI nanofibers is formed between the graphene and PDI, which enhances the long-range π-electrons delocalization and electron coupling effects, and then it is beneficial for the carrier mobility [53,54]. In addition, the Raman peak of the composite at 1561 cm^{-1} shows a shift compared to that of PDI (1582 cm^{-1}), which further indicates that the existence of π-π interaction between graphene and PDI.

Fig. 2(B) shows the Fourier transform infrared (FT-IR) spectra of PDI and rGO/PDI composite. The peak of PDI at 1651 cm^{-1} is attributed to the C=C stretching vibrations [24]. Interestingly, it can be clearly seen that the infrared absorption peaks of rGO/PDI has a red shift compared to pure PDI, which indicates the increase of the conjugated structure in rGO/PDI. It is further demonstrated that the existence of π-π interaction between graphene and PDI.

To further illustrate the chemical state of the sample, XPS was carried out. As shown in Fig. 3, the C 1 s of rGO exhibits binding energy peaks at 284.7 eV, 286.7 eV, and 289.1 eV, which correspond to sp^2 carbon C=C, −C−O, and C=O, respectively [55–58]. It indicates that there are still certain amounts of the oxygen-containing functional groups on the surface of rGO, and their hydrophilicity is favorable for the photocatalytic reaction. The extra C−N peak in rGO/PDI is mainly derived from PDI. It can be seen that the C=C peak at 284.4 eV of rGO/PDI is shifted by 0.2 eV toward low binding energy compared to pure PDI (284.6 eV), which is mainly attributed to the increase of electron density induced by π-π interaction between graphene and PDI. It indicates that the addition of rGO extends the π-conjugation of PDI through the π−π interaction and obviously increases the electron density [55]. The peak fitting analysis data of C 1 s are shown in table S1. It can be seen that the C=C content of rGO/PDI (~73.87%) is higher than the individual PDI (~61.62%). The result clearly indicates that the introduction of rGO increases the C=C bond intensity. In addition, the Fig. 3(D) shows that the N 1 s peak of rGO/PDI (399.2 eV) is shifted by 0.4 eV toward low binding energy compared to pure PDI (399.6 eV), which further implies the existence of π-π interaction between graphene and PDI.

3.1.1. The three-dimensional network structure

Fig. 4 shows the SEM images of samples and the TEM is shown in the supporting documents (Fig. S1). It can be seen that the pure PDI generates obvious agglomeration (Fig. 4A) and it exhibits a typical one-dimensional nanofiber structure (Fig. S1A). The rGO presents a three-dimensional network structure and the ultrathin graphene sheets cross-link together (Figs. 4B and S1 B). The SEM pictures of rGO/PDI composite (Fig. 4C and D) show that the self-assembled PDI nanofibers are dispersed in the three-dimensional network structure of the graphene. The results indicate that graphene does not affect the orderly self-assembly of PDI and it in turn improves the dispersion of PDI. More importantly, the 3D structure can provide multi-dimensional channels for electron transport, which is very favorable for photocatalytic reactions [39]. The high-resolution transmission of rGO/PDI (Fig. S1 D) further suggests that PDI is sufficiently integrated with graphene sheet. The close interfacial effect is mainly attributed to the non-covalent π-π interaction between graphene and PDI, which is beneficial to the electron transfer.

The atomic force is further investigated as shown in Fig. 5. The result shows that graphene presents a very thin layer with a thickness of 0.3 ~ 0.4 nm (Fig. 5A). The self-assembled PDI shows the one-dimensional nanofiber morphology (Fig. 5B), which is stacked in several layers and the thickness of a single sheet is mainly distributed around

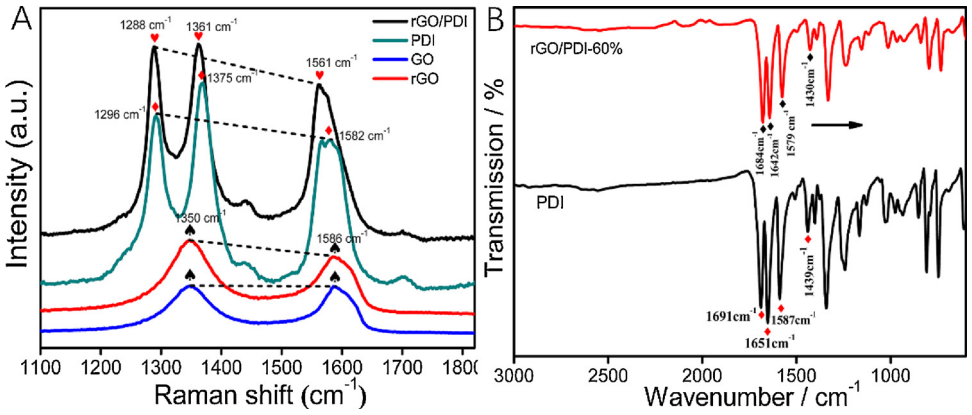

Fig. 2. (A) Raman spectra and (B) FT-IR spectra of PDI and rGO/PDI aerogel composite.

7 nm–10 nm. It indicates that the individual PDI is prone to agglomeration, which is accordant with the result of SEM in Fig. 4A. As for rGO/PDI, the three-dimensional photograph (Fig. 5C) vividly shows that rGO and PDI are closely knit together. The layer thickness of rGO/PDI is about 7 nm, which is similar to the monolayer of PDI. This further indicates that graphene improves the dispersion of PDI.

For rGO/PDI composite, the separation of photo-generated carriers mainly occurs at the interface between graphene and the central catalyst PDI, so increasing the interfacial contact will facilitate the separation of photo-generated carriers. As shown in SEM, TEM and AFM, it can be concluded that the three-dimensional network structure improves the dispersion of PDI and facilitates the close interface contact effect, which is essential for the improvement of photocatalytic performance.

In addition, Fig. S2 shows the UV–vis diffuse reflectance spectra of the samples. The absorption edges of PDI is about 738 nm, corresponding to the bandgap of 1.68 eV, which indicates that it can be easily excited by visible light. It is obvious that the addition of graphene enhances the ability of visible light absorption of PDI and induces significant red shift, which is also favorable for the photocatalytic reaction. Fig. S3 presents the N_2 adsorption-desorption isotherms of the samples, the result shows that the specific surface area of rGO/PDI composites increases at different degree compared to pure PDI. The larger specific surface area can promote the adsorption ability of the catalysts and provide more reactive sites for the photocatalytic reaction. Thus it can be seen that the advantages of the three-dimensional structure in the photocatalytic degradation are manifold.

3.2. Photocatalytic activity in static system

The adsorption capabilities of samples are shown in Fig. S4 (Supporting information). As shown in Fig. S4, it took about one hour to get adsorption equilibrium and the adsorption capacity of rGO/PDI composite was much better than that of pure PDI. This indicates that

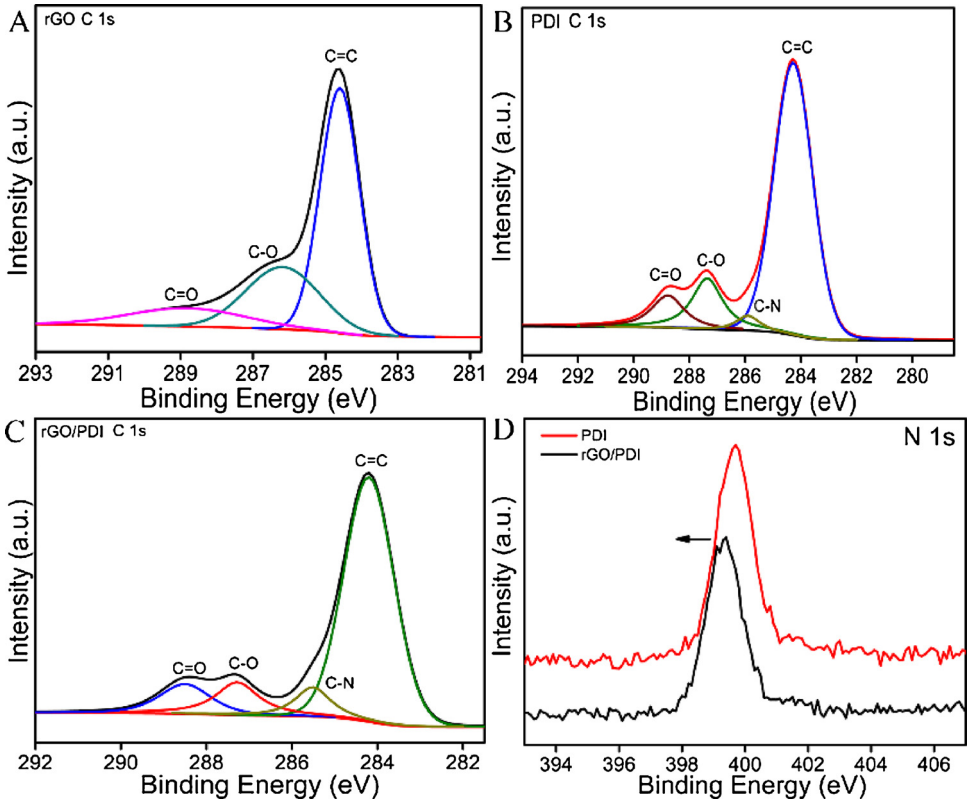

Fig. 3. The high-resolution regional spectra of C 1 s orbital of (A) rGO, (B) PDI and (C) rGO/PDI and (D) the XPS spectra of N1 s orbital of PDI and rGO/PDI.

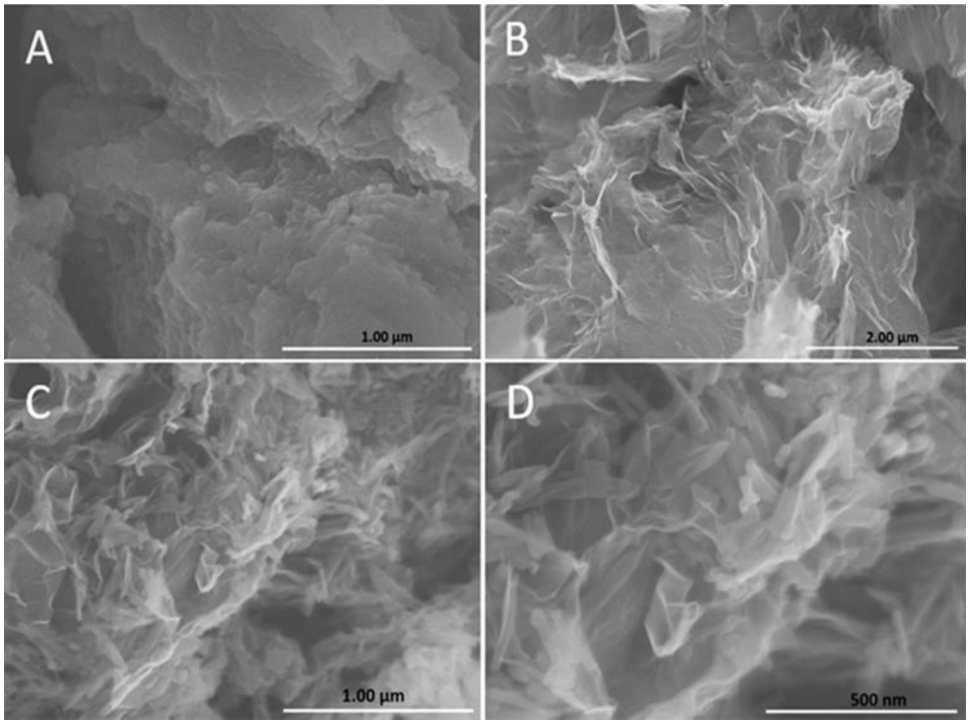

Fig. 4. SEM images of (A) PDI, (B) rGO and (C, D) rGO/PDI-60% composite aerogel.

the three-dimensional network structure is beneficial to increase the adsorption and enrichment ability of the pure PDI, which is critical to the subsequent photocatalytic reaction.

The visible-light photocatalytic performance of samples is evaluated after adsorption equilibrium. As shown in Fig. 6(A), the pure PDI showed a relatively low activity in degrading phenol. Interestingly, the photocatalytic activity of rGO/PDI composite was enhanced gradually with the increasing mass ratio of PDI. When the mass fraction of PDI reached sixty percent, it exhibited the highest photocatalytic activity. The apparent rate constant k of rGO/PDI-60% is 0.465 h^{-1}, which is almost 2.46 times as high as that of PDI (0.189 h^{-1}). As shown in Fig. 6(B), the peak located at 3.169 min corresponds to phenol and the

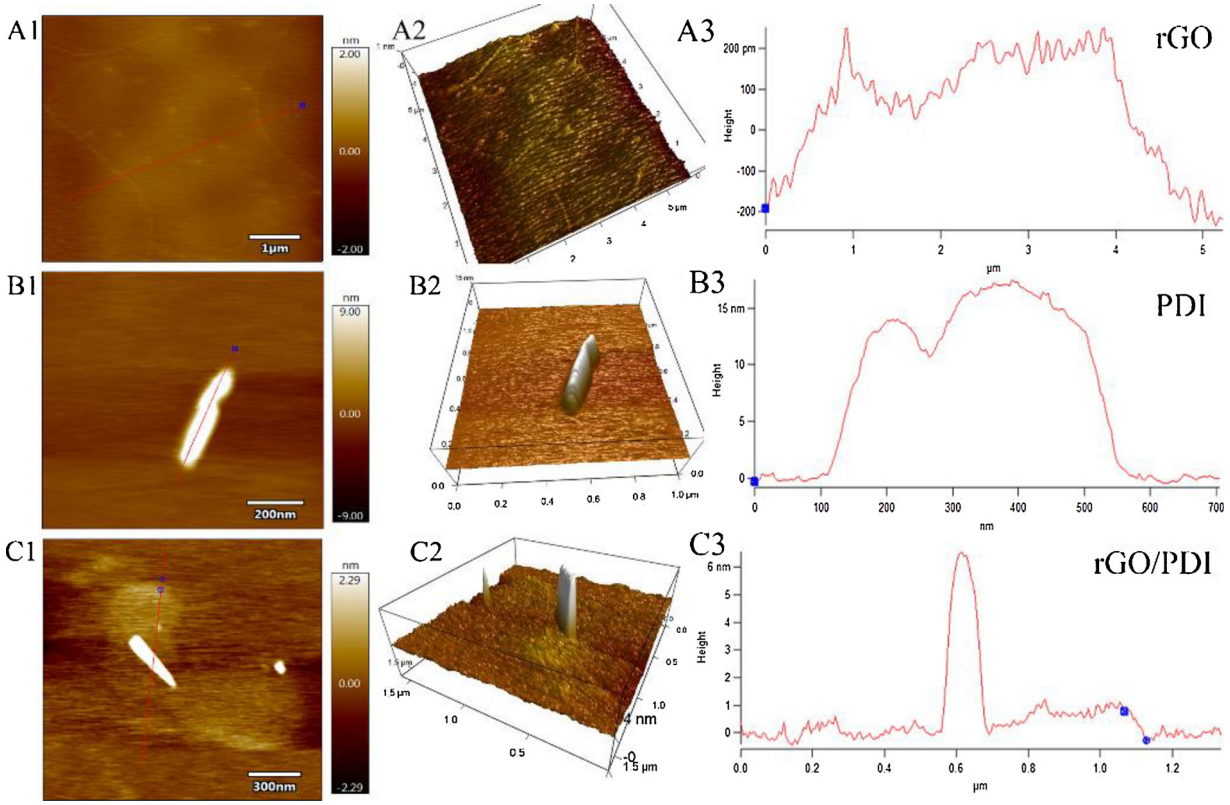

Fig. 5. Atomic force micrograph (AFM) of (A) rGO, (B) PDI, and (C) rGO/PDI-60%.

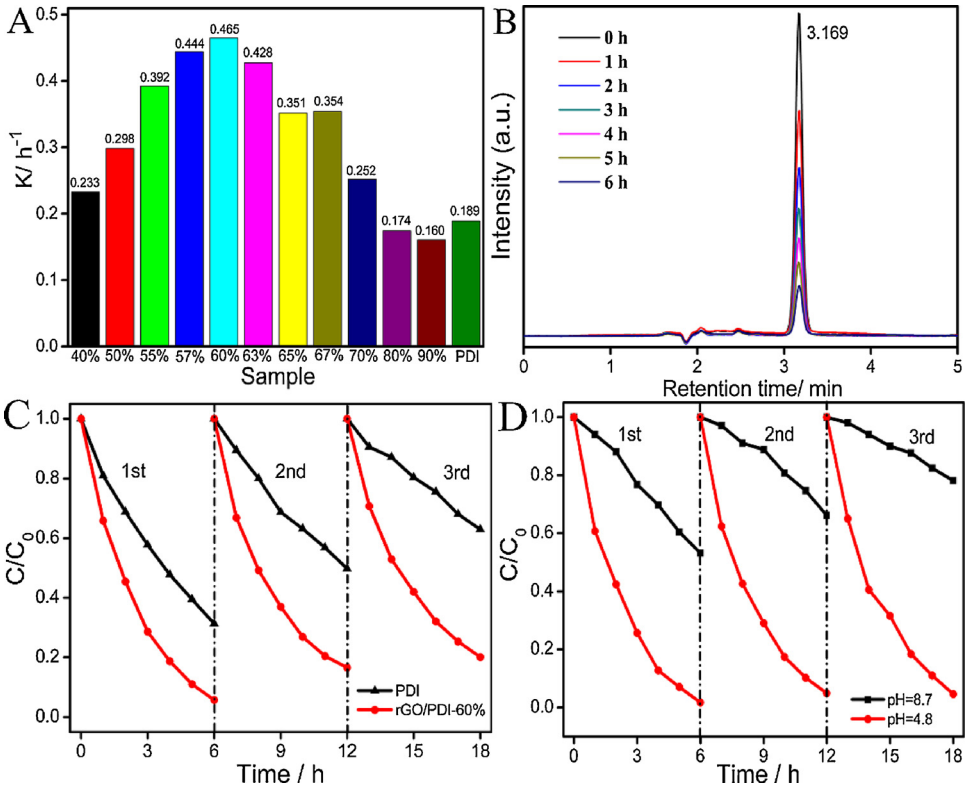

Fig. 6. (A) The degradation rate constants *k* of samples for phenol degradation; (B) HPLC spectrums of phenol solution degraded by rGO/PDI-60% composite; (C) Recycling tests of PDI and rGO/PDI-60% for phenol degradation in the neutral environment; (D) Recycling tests of rGO/PDI-60% for phenol degradation in the acid (pH = 4.8) and alkaline (pH = 8.7) environment.

HPLC results showed that the concentration of phenol gradually decreased with continuous irradiation. Few intermediate species and PDI were detected, indicating that the dissolution of PDI in the composite structure was very few and phenol was mineralized to CO_2.

The stability of PDI is an important issue in the photodegradation reaction. As shown in Fig. 6(C), the rGO/PDI composite remained higher stability than the pure PDI in neutral environment. Furthermore, the catalytic stability of rGO/PDI was also investigated in the acid and alkaline environment (Fig. 6D). The results indicated that the rGO/PDI composite has higher stability in the acid environment than in the neutral and alkaline environment. The decreased activity at neutral and alkaline solution could be attributed to the depolymerization of PDI during the photodegradation [24].

The activity of rGO/PDI composite was further investigated compared with other reported typical visible-light photocatalysts. As shown in Fig. S6, for phenol degradation, the activity of rGO/PDI-60% is 5.93, 16.06, 3.15, 2.11 times higher than that of Bi_2WO_6, g-C_3N_4, bulk PDI, and commercial self-assembly PDI, respectively. In addition, 2, 4-Dichlorophenol have also been used as the probe molecule to evaluate the activity. The results showed that rGO/PDI also had the best activity than other catalysts.

3.3. The synergetic effect of adsorption and photocatalysis in Dynamic System

The synergetic effect of adsorption and photocatalysis was investigated in a dynamic system, namely, the peristaltic pump and the light source were turned on at the same time in the photocatalytic test [38]. As shown in Fig. 7(A), the degradation rate of rGO/PDI composite for methylene blue (MB) degradation was 3.33 times as high as that of PDI after light irradiation for ten hours. This fully demonstrates that rGO/PDI composite has the synergistic effect between adsorption and photocatalysis in the photocatalytic degradation. As for the rGO/PDI composite, the three-dimensional network structure of graphene improves the adsorption ability for pollutants. It is worth noting that the photocatalytic performance of PDI is significantly reduced with the continuous reaction, while the rGO/PDI composite exhibits satisfactory photocatalytic stability. It further indicates that the addition of graphene improves the stability of PDI. The maximum absorption peak of MB can be seen at 663 nm, which gradually decreases from 0 min to 80 min, which indicates that the concentration of MB decreases with irradiation time.

3.4. Mechanism of photocatalytic activity enhancement

The transient photocurrent and photoluminescence characterization were used to analyze the separation and migration efficiency of photo-generated carriers. As shown in Fig. 8(A), PDI and rGO/PDI composite both showed a relatively stable instantaneous photocurrent signal. However, the photocurrent intensity of rGO/PDI (3.2 μA) is about 13 times higher than that of PDI (0.25 μA). It indicated that the addition of graphene facilitated the separation and transmission of photo-generated carriers. It is not only attributed to the excellent conductivity of graphene, but more importantly, the close π-π interaction between graphene and PDI promotes the electron delocalization and the three-dimensional structures provides a fast channel for the electron transfer. As shown in Fig. 8(B), the self-assembled PDI has a strong emission peak at 733 nm, which is mainly due to the recombination of photo-generated electrons and holes. However, the fluorescence intensity of the rGO/PDI composite was obviously weakened, which further demonstrated that the separation and transmission of photon-generated carriers are enhanced after the addition of graphene.

In addition, the rGO/PDI-60% composite shows higher photocatalytic performance than the physical mixture (the mass fraction of PDI is 60%) as shown in Fig. S7, which indicates that the π-π interaction between graphene and PDI is the main factor for the photocatalytic activity enhancement.

Active species plays a crucial role in the photocatalytic reaction, so what kind of active species dominates the photo-degradation reaction? The free radical trapping experiment was conducted. The experimental details were shown in the supporting documents. As shown in Fig. 9, formic acid, tert-butyl alcohol, and benzoquinone are used as the

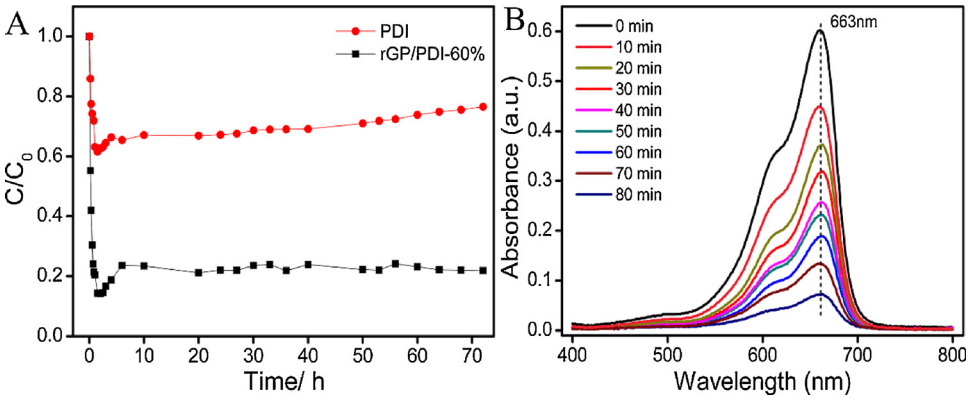

Fig. 7. (A) Adsorption and photocatalytic degradation synergistic removal of MB by PDI and rGO/PDI-60% composite with 3.5 mL/min flow rate in dynamic system; (B) the UV absorbance of methylene blue with time (from 0 min to 80 min). (For interpretation of the references to colour in this figure legend, the reader is referred to the web version of this article).

trapping agents for holes (h^+), hydroxyl radicals (OH), and superoxide radicals ($O_2^{\cdot -}$), respectively. The result shows that the photo-degradation of phenol was apparently inhibited when formic acid was added. This phenomenon gives evidence that the degradation of phenol is dominated by the direct hole oxidation. On the other hand, it can be seen that the photocatalytic performance reduced to some extent after adding tert-butyl alcohol and benzoquinone, indicating OH and $O_2^{\cdot}$- also participate in the photocatalytic degradation. The electron spin resonance (ESR) measurement were further performed to detect OH and $O_2^{\cdot}$-. As shown in Fig. S8, there was no signal response in the absence of light. However, obvious signals appear after illumination, which further indicated that OH and $O_2^{\cdot}$- indeed play a role in the photocatalytic process.

Based on the above discussion, the photocatalytic degradation mechanism of the aerogel composite was proposed, which was shown in Fig. 10. Firstly, the self-assembled PDI and 3D graphene are effectively combined via non-covalent π-π interaction. The central catalytic component PDI will be excited under the irradiation of visible light as its narrow bandgap (1.68 eV). And then the electrons and holes can be respectively generated in the conduction band (−0.17 eV *vs*. NHE) and valence band (1.52 eV vs. NHE) [24]. The enlargement of electron delocalization effect induced by π-π interaction is beneficial to facilitate charge transfer. The excellent electrical conductivity of graphene and the three-dimensional structure also provide a fast multidimensional channel for electron transfer. So the photo-generated electrons on the conduction band of PDI can easily transferred to the graphene sheet, which will further react with dissolved oxygen in water to form superoxide radicals. Superoxide radicals have strong oxidation capacity, which can decompose or even mineralize organic pollutants. The high-speed electron transfer promotes the separation efficiency of carriers, making the photo-generated holes effectively participate in the photocatalytic reaction. On the one hand, the photo-generated holes can directly mineralize organic contaminants. On the other hand, h^+ can

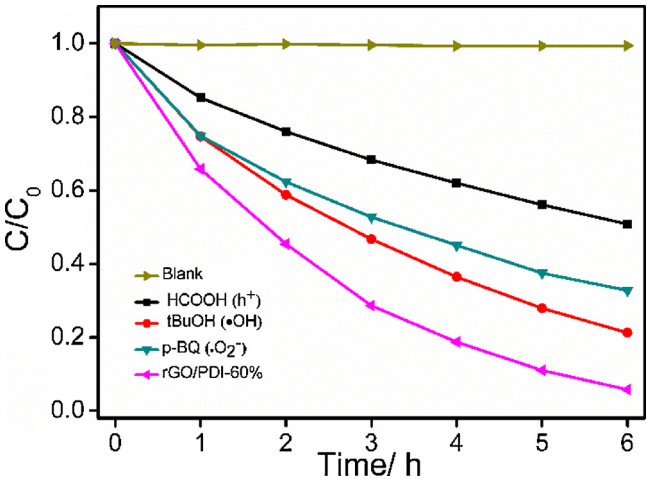

Fig. 9. Effects of different scavengers on phenol degradation in the presence of rGO/PDI-60% under visible light irradiation.

combine with hydroxyl in water to generate OH according to the ESR result and then organic pollutants can be decomposed by OH. The photocatalytic mechanism further indicates that the π-π interaction, three-dimensional structure and excellent conductivity of graphene play a crucial synergetic role in the electron transfer process of photocatalytic reactions.

4. Conclusion

In conclusion, a three-dimensional graphene/self-assembled perylene imide (rGO/PDI) aerogel composite has been successfully constructed via a simple low-temperature hydrothermal method. Graphene and PDI are effectively combined via non-covalent π-π interaction. The

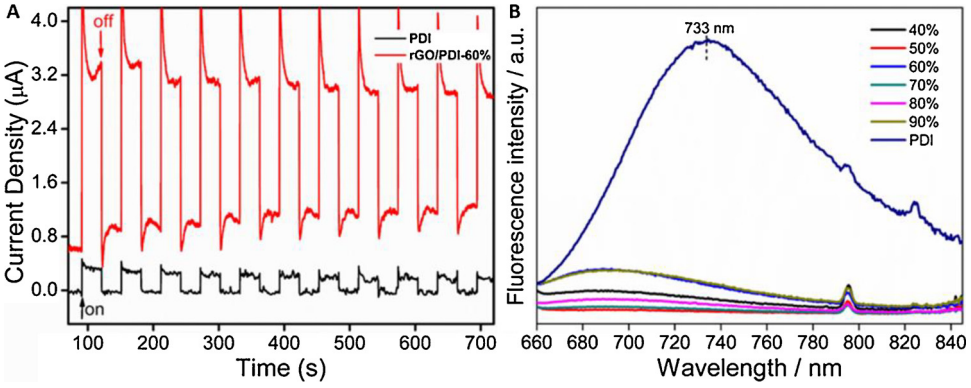

Fig. 8. (A) Photocurrents of PDI and rGO/PDI-60% under the irradiation of visible light and (B) Photoluminescence spectra of pure PDI and rGO/PDI composites.

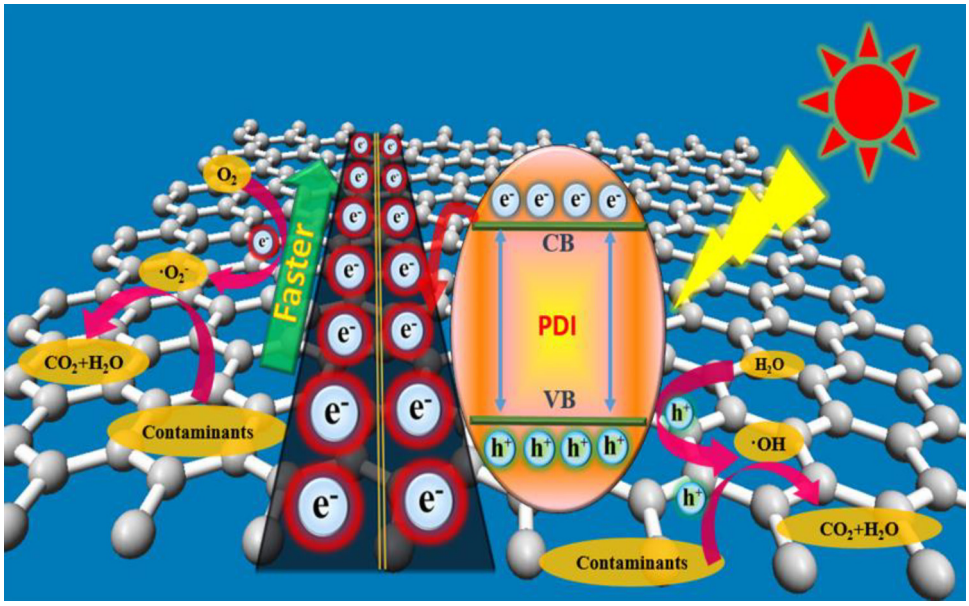

Fig. 10. Schematic diagram of electron–hole pairs' separation process and the photocatalytic process under visible light (λ > 420 nm).

three-dimensional aerogel composite exhibits satisfactory photocatalytic performance and stability in static and dynamic catalytic systems. On the one hand, the close π-π interaction and the excellent conductivity of graphene facilitate the separation of charge carriers. On the other hand, the three-dimensional network structure improves the dispersion of PDI and provides a high-speed multidimensional channel for electron transfer. Finally, hole (h^+) mainly dominates the photodegradation reaction.

Acknowledgements

This work was partly supported by Chinese National Science Foundation (21437003, 21673126, 21761142017, 21621003) and Collaborative Innovation Center for Regional Environmental Quality.

Appendix A. Supplementary data

Supplementary material related to this article can be found, in the online version, at doi:https://doi.org/10.1016/j.apcatb.2018.09.003.

References

[1] C. Chen, W. Ma, J. Zhao, Semiconductor-mediated photodegradation of pollutants under visible-light irradiation, Chem. Soc. Rev. 39 (2010) 4206–4219.
[2] L. Zhao, X. Chen, X. Wang, Y. Zhang, W. Wei, Y. Sun, M. Antonietti, M.M. Titirici, One-step solvothermal synthesis of a carbon@TiO(2) dyade structure effectively promoting visible-light photocatalysis, Adv. Mater. 22 (2010) 3317–3321.
[3] Y. Wang, R. Shi, J. Lin, Y. Zhu, Enhancement of photocurrent and photocatalytic activity of ZnO hybridized with graphite-like C3N4, Energy Environ. Sci. 4 (2011) 2922.
[4] H. Liu, J.B. Joo, M. Dahl, L. Fu, Z. Zeng, Y. Yin, Crystallinity control of TiO_2 hollow shells through resin-protected calcination for enhanced photocatalytic activity, Energy Environ. Sci. 8 (2015) 286–296.
[5] J. Yang, R. Hu, W. Meng, Y. Du, A novel p-$LaFeO_3$/n-Ag_3PO_4 heterojunction photocatalyst for phenol degradation under visible light irradiation, Chem. Commun. (Camb.) 52 (2016) 2620–2623.
[6] Y.B. Huang, J. Liang, X.S. Wang, R. Cao, Multifunctional metal-organic framework catalysts: synergistic catalysis and tandem reactions, Chem. Soc. Rev. 46 (2017) 126–157.
[7] A. Kudo, Y. Miseki, Heterogeneous photocatalyst materials for water splitting, Chem. Soc. Rev. 38 (2009) 253–278.
[8] C. Wang, Z. Xie, K.E. deKrafft, W. Lin, Doping metal-organic frameworks for water oxidation, carbon dioxide reduction, and organic photocatalysis, J. Am. Chem. Soc. 133 (2011) 13445–13454.
[9] J. Qiu, X. Zhang, Y. Feng, X. Zhang, H. Wang, J. Yao, Modified metal-organic frameworks as photocatalysts, Appl. Catal. B 231 (2018) 317–342.
[10] C.-C. Wang, J.-R. Li, X.-L. Lv, Y.-Q. Zhang, G. Guo, Photocatalytic organic pollutants degradation in metal–organic frameworks, Energy Environ. Sci. 7 (2014) 2831–2867.
[11] J. Zhang, X. Chen, K. Takanabe, K. Maeda, K. Domen, J.D. Epping, X. Fu, M. Antonietti, X. Wang, Synthesis of a carbon nitride structure for visible-light catalysis by copolymerization, Angew. Chem. Int. Ed. Engl. 49 (2010) 441–444.
[12] K. Schwinghammer, B. Tuffy, M.B. Mesch, E. Wirnhier, C. Martineau, F. Taulelle, W. Schnick, J. Senker, B.V. Lotsch, Triazine-based carbon nitrides for visible-light-driven hydrogen evolution, Angew. Chem. Int. Ed. Engl. 52 (2013) 2435–2439.
[13] L. Kong, Y. Ji, Z. Dang, J. Yan, P. Li, Y. Li, S.F. Liu, G-C3N4 loading black phosphorus quantum dot for efficient and stable photocatalytic H2 generation under visible light, Adv. Funct. Mater. (2018) 1800668.
[14] H. Bian, Y. Ji, J. Yan, P. Li, L. Li, Y. Li, S. Frank Liu, In situ synthesis of few-layered g-C_3N_4 with vertically aligned MoS2 loading for boosting solar-to-Hydrogen generation, Small 14 (2018).
[15] G.S. Thool, K. Narayanaswamy, A. Venkateswararao, S. Naqvi, V. Gupta, S. Chand, V. Vivekananthan, R.R. Koner, V. Krishnan, S.P. Singh, Highly directional 1D supramolecular assembly of new diketopyrrolopyrrole-based gel for organic solar cell applications, Langmuir 32 (2016) 4346–4351.
[16] C. Fu, P.J. Beldon, D.F. Perepichka, H-bonding control of supramolecular ordering of diketopyrrolopyrroles, Chem. Mater. 29 (2017) 2979–2987.
[17] P. Guo, P. Chen, W. Ma, M. Liu, Morphology-dependent supramolecular photocatalytic performance of porphyrin nanoassemblies: from molecule to artificial supramolecular nanoantenna, J. Mater. Chem. 22 (2012) 20243–20249.
[18] C. Zhang, P. Chen, H. Dong, Y. Zhen, M. Liu, W. Hu, Porphyrin supramolecular 1D structures via surfactant-assisted self-assembly, Adv. Mater. 27 (2015) 5379–5387.
[19] M. Más-Montoya, R.A. Janssen, The eff ;ect of H-and J-aggregation on the photophysical and photovoltaic properties of small thiophene–pyridine–dpp molecules for bulk-heterojunction solar cells, Adv. Funct. Mater. 27 (2017).
[20] A.S. Weingarten, R.V. Kazantsev, L.C. Palmer, M. McClendon, A.R. Koltonow, A.P. Samuel, D.J. Kiebala, M.R. Wasielewski, S.I. Stupp, Self-assembling hydrogel scaffolds for photocatalytic hydrogen production, Nat. Chem. 6 (2014) 964–970.
[21] A.S. Weingarten, R.V. Kazantsev, L.C. Palmer, D.J. Fairfield, A.R. Koltonow, S.I. Stupp, Supramolecular packing controls H_2 photocatalysis in chromophore amphiphile hydrogels, J. Am. Chem. Soc. 137 (2015) 15241–15246.
[22] D. Liu, J. Wang, X. Bai, R. Zong, Y. Zhu, Self-assembled PDINH supramolecular system for photocatalysis under visible light, Adv. Mater. 28 (2016) 7284–7290.
[23] W. Wei, D. Liu, Z. Wei, Y. Zhu, Short-range π–π stacking assembly on P25 TiO_2 nanoparticles for enhanced visible-light photocatalysis, ACS Catal. 7 (2016) 652–663.
[24] J. Wang, W. Shi, D. Liu, Z. Zhang, Y. Zhu, D. Wang, Supramolecular organic nanofibers with highly efficient and stable visible light photooxidation performance, Appl. Catal. B 202 (2017) 289–297.
[25] K. Zhang, J. Wang, W. Jiang, W. Yao, H. Yang, Y. Zhu, Self-assembled perylene diimide based supramolecular heterojunction with Bi2WO6 for efficient visible-light-driven photocatalysis, Appl. Catal. B 232 (2018) 175–181.
[26] W. Wei, Z. Wei, D. Liu, Y. Zhu, Enhanced visible-light photocatalysis via back-electron transfer from palladium quantum dots to perylene diimide, Appl. Catal. B 230 (2018) 49–57.
[27] J. Wang, D. Liu, Y. Zhu, S. Zhou, S. Guan, Supramolecular packing dominant photocatalytic oxidation and anticancer performance of PDI, Appl. Catal. B 231 (2018) 251–261.
[28] Z. Zhang, J. Wang, D. Liu, W. Luo, M. Zhang, W. Jiang, Y. Zhu, Highly efficient organic photocatalyst with full visible light Spectrum through pi-pi stacking of TCNQ-PTCDI, ACS Appl. Mater. Interfaces 8 (2016) 30225–30231.

[29] A. Dasgupta, L.P. Rajukumar, C. Rotella, Y. Lei, M. Terrones, Covalent three-dimensional networks of graphene and carbon nanotubes: synthesis and environmental applications, Nano Today 12 (2017) 116–135.
[30] Q. Li, B. Quan, W. Li, J. Lu, J. Zheng, X. Yu, J. Li, H. Li, Electro-plating and stripping behavior on lithium metal electrode with ordered three-dimensional structure, Nano Energy 45 (2018) 463–470.
[31] X. Wang, A. Liu, Y. Xing, H. Duan, W. Xu, Q. Zhou, H. Wu, C. Chen, B. Chen, Three-dimensional graphene biointerface with extremely high sensitivity to single cancer cell monitoring, Biosens. Bioelectron. 105 (2018) 22–28.
[32] X. Wang, Q. Liu, Q. Yang, Z. Zhang, X. Fang, Three-dimension g-C_3N_4 aggregate composed of hollow bubbles with high activity for photocatalytic degradation of tetracycline, Carbon 136 (2018) 103–112.
[33] B. Qiu, M. Xing, J. Zhang, Mesoporous TiO_2 nanocrystals grown in situ on graphene aerogels for high photocatalysis and lithium-ion batteries, J. Am. Chem. Soc. 136 (2014) 5852–5855.
[34] C. Hou, Q. Zhang, Y. Li, H. Wang, P25-graphene hydrogels: room-temperature synthesis and application for removal of methylene blue from aqueous solution, J. Hazard. Mater. 205-206 (2012) 229–235.
[35] W. Jiang, W. Luo, R. Zong, W. Yao, Z. Li, Y. Zhu, Polyaniline/carbon nitride nanosheets composite hydrogel: a separation-free and high-efficient photocatalyst with 3D hierarchical structure, Small 12 (2016) 4370–4378.
[36] M. Zhang, W. Jiang, D. Liu, J. Wang, Y. Liu, Y. Zhu, Y. Zhu, Photodegradation of phenol via C_3N_4-agar hybrid hydrogel 3D photocatalysts with free separation, Appl. Catal. B 183 (2016) 263–268.
[37] M. Zhang, W. Luo, Z. Wei, W. Jiang, D. Liu, Y. Zhu, Separation free C_3N_4/SiO_2 hybrid hydrogels as high active photocatalysts for TOC removal, Appl. Catal. B 194 (2016) 105–110.
[38] W. Jiang, Y. Liu, J. Wang, M. Zhang, W. Luo, Y. Zhu, Separation-free Polyaniline/TiO_2 3D hydrogel with high photocatalytic activity, Adv. Mater. Interfaces 3 (2016) 1500502.
[39] X. Chen, Q. Chen, W. Jiang, Z. Wei, Y. Zhu, Separation-free TiO_2-graphene hydrogel with 3D network structure for efficient photoelectrocatalytic mineralization, Appl. Catal. B 211 (2017) 106–113.
[40] B. Qiu, M. Xing, J. Zhang, Recent advances in three-dimensional graphene based materials for catalysis applications, Chem. Soc. Rev. 47 (2018) 2165–2216.
[41] F. Chen, W. An, L. Liu, Y. Liang, W. Cui, Highly efficient removal of bisphenol A by a three-dimensional graphene hydrogel-AgBr@rGO exhibiting adsorption/photocatalysis synergy, Appl. Catal. B 217 (2017) 65–80.
[42] C. Mu, Y. Zhang, W. Cui, Y. Liang, Y. Zhu, Removal of bisphenol A over a separation free 3D Ag_3 PO_4 -graphene hydrogel via an adsorption-photocatalysis synergy, Appl. Catal. B 212 (2017) 41–49.
[43] F. Chen, W. An, Y. Li, Y. Liang, W. Cui, Fabricating 3D porous PANI/TiO_2–graphene hydrogel for the enhanced UV-light photocatalytic degradation of BPA, Appl. Surf. Sci. 427 (2018) 123–132.
[44] W.S. Hummers Jr, R.E. Offeman, Preparation of graphitic oxide, J. Am. Chem. Soc. 80 (1958) 1339.
[45] P. He, J. Sun, S. Tian, S. Yang, S. Ding, G. Ding, X. Xie, M. Jiang, Processable aqueous dispersions of graphene stabilized by graphene quantum dots, Chem. Mater. 27 (2014) 218–226.
[46] R. Wang, K.-Q. Lu, F. Zhang, Z.-R. Tang, Y.-J. Xu, 3D carbon quantum dots/graphene aerogel as a metal-free catalyst for enhanced photosensitization efficiency, Appl. Catal. B 233 (2018) 11–18.
[47] J. Qian, J. Yan, C. Shen, F. Xi, X. Dong, J. Liu, Graphene quantum dots-assisted exfoliation of graphitic carbon nitride to prepare metal-free zero-dimensional/two-dimensional composite photocatalysts, J. Mater. Sci. 53 (2018) 12103–12114.
[48] Y. Xu, K. Sheng, C. Li, G. Shi, Self-assembled graphene hydrogel via a one-step hydrothermal process, ACS Nano 4 (2010) 4324–4330.
[49] W. Lv, C. Zhang, Z. Li, Q.H. Yang, Self-assembled 3D graphene monolith from solution, J. Phys. Chem. Lett. 6 (2015) 658–668.
[50] A. Datar, K. Balakrishnan, L. Zang, One-dimensional self-assembly of a water soluble perylene diimide molecule by pH triggered hydrogelation, Chem. Commun. (Camb.) 49 (2013) 6894–6896.
[51] X. Yang, H. Cui, Y. Li, J. Qin, R. Zhang, H. Tang, Fabrication of $Ag3PO_4$-Graphene composites with highly efficient and stable visible light photocatalytic performance, ACS Catal. 3 (2013) 363–369.
[52] M. Angelella, C. Wang, M.J. Tauber, Resonance Raman spectra of a perylene bis (dicarboximide) chromophore in ground and lowest triplet states, J. Phys. Chem. A 117 (2013) 9196–9204.
[53] M.X. Zhang, G.J. Zhao, Modification of n-type organic semiconductor performance of perylene diimides by substitution in different positions: two-dimensional pi-stacking and hydrogen bonding, ChemSusChem 5 (2012) 879–887.
[54] C. Xavier, C. Jérôme, F. Rainer, K.K. Okudaira, V. Lemaur, A. Crispin, G. Kestemont, M. Lehmann, M. Fahlman, R. Lazzaroni, Y. Geerts, G. Wendin, N. Ueno, J. Bre´das, W.R. Salaneck, Electronic delocalization in discotic liquid crystals: a joint experimental and theoretical study, J. Am. Chem. Soc. 126 (2004) 11889.
[55] P. Karthik, R. Vinoth, P. Zhang, W. Choi, E. Balaraman, B. Neppolian, Π–π interaction between metal–Organic framework and reduced graphene oxide for visible-light photocatalytic H_2 production, Acs Appl. Energy Mater. 1 (5) (2018) 1913–1923.
[56] D. Xu, B. Cheng, W. Wang, C. Jiang, J. Yu, Ag_2CrO_4/g-C_3N_4/graphene oxide ternary nanocomposite Z-scheme photocatalyst with enhanced CO_2 reduction activity, Appl. Catal. B 231 (2018) 368–380.
[57] Q. Cheng, J. Xu, T. Wang, L. Fan, R. Ma, X. Yu, J. Zhu, Z. Xu, B. Lu, Double quantum dots decorated 3D graphene flowers for highly efficient photoelectrocatalytic hydrogen production, Appl. Surf. Sci. 422 (2017) 528–535.
[58] Y. Zhao, X. Zhang, C. Wang, Y. Zhao, H. Zhou, J. Li, H. Jin, The synthesis of hierarchical nanostructured MoS_2/Graphene composites with enhanced visible-light photo-degradation property, Appl. Surf. Sci. 412 (2017) 207–213.